Quaternary Science Reviews 42 (2012) 29–42

Contents lists available at SciVerse ScienceDirect

Quaternary Science Reviews

journal homepage: www.elsevier.com/locate/quascirev

Estimating coseismic coastal uplift with an intertidal mussel: calibration for the 2010 Maule Chile earthquake ($M_w = 8.8$)

Daniel Melnick [a,*], Marco Cisternas [b], Marcos Moreno [c], Ricardo Norambuena [d]

[a] Institut für Erd- und Umweltwissenschaften, DFG Leibniz Center for Surface Process and Climate Studies, Universität Potsdam, 14415 Potsdam, Germany
[b] Escuela de Ciencias del Mar, Pontificia Universidad Católica de Valparaíso, 1020 Valparaíso, Chile
[c] Helmholtz Zentrum Potsdam, 14473 Potsdam, Germany
[d] UNESCO Coastal Programs, 7511019 Santiago, Chile

ARTICLE INFO

Article history:
Received 16 August 2011
Received in revised form
15 March 2012
Accepted 23 March 2012
Available online 25 April 2012

Keywords:
Coastal uplift
Maule earthquake
Chile
Intertidal organisms
Perumytilus mussels
Slip distribution

ABSTRACT

Coseismic coastal uplift has been quantified using sessile intertidal organisms after several great earthquakes following FitzRoy's pioneer measurements in 1835. A dense survey of such markers may complement space geodetic data to obtain an accurate distribution of fault slip and earthquake segmentation. However, uplift estimates based on diverse intertidal organisms tend to differ, because of few methodological and comparative studies. Here, we calibrate and estimate coastal uplift in the southern segment of the 2010 Maule, Chile earthquake ($M_w = 8.8$) using >1100 post-earthquake elevation measurements of the sessile mussel *Perumytilus purpuratus*. This mussel is the predominant competitor for rocky shores all along the Pacific coast of South America, where it forms fringes or belts distinctively in the middle intertidal zone. These belts are centered at mean sea level and their width should equal one third of the tidal range. We measured belt widths close to this value at 40% of the sites, but overall widths are highly variable due to the unevenness in belt tops; belt bases, in turn, are rather regular. Belt top unevenness apparently results from locally-enhanced wave splash, whereas belt base evenness is controlled by predation. According to our measurements made beyond the earthquake rupture, the belt base is at the bottom of the middle intertidal zone, and thus we propose to estimate coastal uplift using the belt base mean elevation plus one sixth of the tidal range to reach mean sea level. Within errors our estimates agree with GPS displacements but differ from other methods. Comparisons of joint inversions for megathrust slip suggest combining space geodetic data with estimates from intertidal organisms may locally increase the detail of slip distributions.

1. Introduction

Sudden coastal uplift and subsidence are commonly associated with earthquakes in a variety of tectonic settings. Robert FitzRoy and Charles Darwin first documented coastal uplift in south-central Chile after the great 1835 earthquake; the immediate predecessor of the 2010 Maule event. Soon after the event, they observed that intertidal sessile organisms had died due to emergence above high tide and FitzRoy measured the amount of uplift using the post-earthquake level of mussels still attached to the rocks (Fitzroy, 1839; Darwin, 1851). Their observations are considered to be the first empirical confirmation of the relation between earthquakes and mountain building (Kölbl-Ebert, 1999).

Following this pioneer work, coseismic coastal land-level changes have been estimated using intertidal organisms in subduction zones, strike-slip fault systems, and continental thrust belts. Land-level changes have been estimated using corals in the tropics (e.g., Briggs et al., 2006; Subarya et al., 2006; Konca et al., 2007; Taylor et al., 2008; Hayes et al., 2010); coralline algae in tropical as well as temperate regions (e.g., Boding and Klinger, 1986; Plafker and Ward, 1992; Carver et al., 1994; Ortlieb et al., 1996; Ramírez-Herrera and Orozco, 2002; Lagabrielle et al., 2003; Meghraoui et al., 2004; Farías et al., 2010); and sessile mollusks in temperate areas (e.g., Plafker, 1965; Plafker and Savage, 1970; Castilla, 1988; Awata et al., 2008; Castilla et al., 2010). However, with the exception of tropical corals, few studies have focused on the distribution of such markers along an uplifted coastline, discussing the influence of local site effects on the accuracy of uplift measurements and the specific methodological aspects that may improve the reliability.

Here we present a systematic study of coastal uplift associated with the 2010 Maule, Chile earthquake of moment magnitude (M_w) 8.8 using a sessile intertidal mussel. We propose a methodology and compare our results with independent estimates from another intertidal organism, benchmarks re-leveling, geodetic Global

* Corresponding author. Tel.: +49 331 977 6252; fax: +49 331 977 5700.
E-mail addresses: melnick@geo.uni-potsdam.de, danmelski@gmail.com (D. Melnick).

0277-3791/$ – see front matter © 2012 Elsevier Ltd. All rights reserved.
doi:10.1016/j.quascirev.2012.03.012

Positioning System (GPS) measurements, a comparison of pre- and post-earthquake high-tide marks, and of pre- and post-earthquake high-resolution topography. We leveled the post-earthquake elevation of the mussel *Perumytilus purpuratus* (Lamarck, 1819) at 33 sites along the southern segment of the Maule rupture zone (Figs. 1 and 2), obtaining a total of 1163 measurements. All the measurements were referred to a mean sea-level datum using tide levels and a tidal model. Based on a statistical analysis of this data set, we propose an approach to estimate coseismic coastal uplift using such mussels focusing on specific aspects that should be considered to reduce the associated uncertainties. The approach has been validated with measurements from two sites located beyond the earthquake rupture. We compare our uplift estimates with independent data and discuss the limitations of each method. Furthermore, we also compare megathrust slip inversions using intertidal organisms and/or space geodetic data and discuss the benefits of combining both data sets to gain insight into the earthquake process.

2. Regional setting: the great 2010 Maule earthquake

On February 27, 2010 at 06:34 UTC time, the Maule earthquake nucleated at the Nazca-South America plate boundary (Fig. 1) reaching $M_w = 8.8$ and becoming the sixth largest event in modern seismology and third in the era of space geodesy, following the 2004 Sumatra and 2011 Japan events. The 2010 Maule rupture extended along an about 500-km-long stretch of south-central Chile involving metric coastal land-level changes and a destructive tsunami averaging 8-m high waves (Farías et al., 2010; Fritz et al., 2011; Vargas et al., 2011). The rupture propagated bilaterally north and southward from the epicenter and finite slip was distributed in two distinct areas centered at 34.5°S and 37.5°S (Fig. 1), reaching a maximum of about 17 m in the northern patch (Tong et al., 2010; Pollitz et al., 2011; Vigny et al., 2011; Moreno et al., 2012). These two areas of high slip apparently correlate with two regions of high pre-seismic plate locking (Moreno et al., 2010).

Slip along the northern patch was located mostly offshore and thus the adjacent coastline subsided, while slip along the southern patch occurred mostly below the coastline resulting in coastal uplift (Figs. 1–3). Because coseismic uplift tends to increase toward the trench, maximum amounts were observed in the southern rupture segment on the Arauco Peninsula, which is only 65 km from the trench (Figs. 1 and 2). In turn, coastal subsidence was reported in the northern segment (Farías et al., 2010) where this distance increases. Maximum coastal uplift of 2.5–3 m has been estimated using intertidal organisms (Castilla et al., 2010; Farías et al., 2010; Vargas et al., 2011) and changes between pre- and post-earthquake high-tide marks (Fritz et al., 2011). However, some

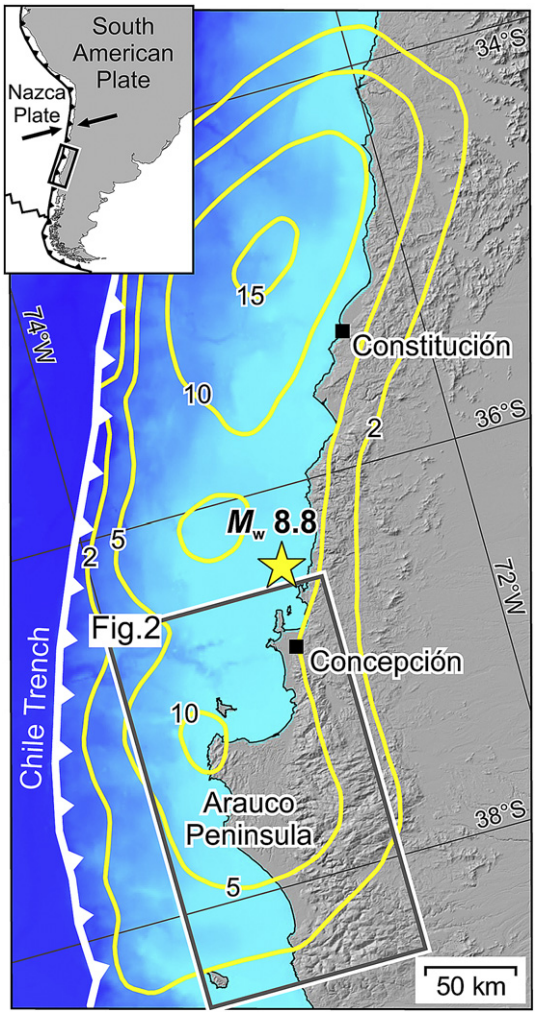

Fig. 1. Tectonic setting of the 2010 Maule, Chile earthquake. Yellow lines show slip contours in meters from Moreno et al. (2012). Slip contours from Moreno et al. (2012). Star shows location of the epicenter from Vigny et al. (2011). (Inset) Tectonic setting of Chile margin, arrows indicate plate convergence at 66 mm/a. (For interpretation of reference to color in this figure, please refer to the web version of this article.)

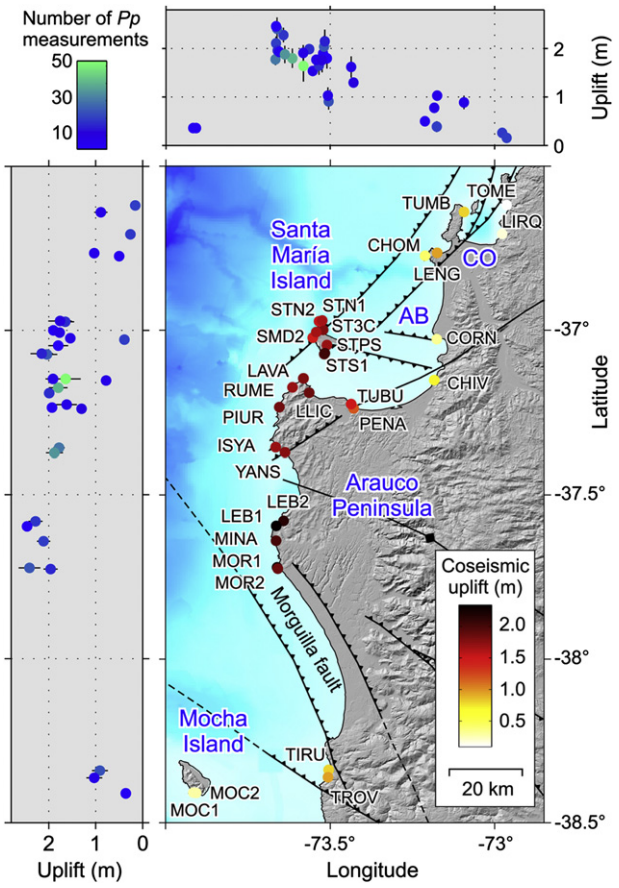

Fig. 2. Coseismic uplift in the southern segment of the 2010 earthquake using *Perumytilus purpuratus* (*Pp*). The color scale in the latitudinal and longitudinal profiles indicates the number of *Pp* belt base measurements used to estimate uplift, see Section 3.2 for details. Quaternary faults from Melnick et al. (2009). AB: Arauco Bay; CO: Concepción. (For interpretation of the references to colour in this figure legend, the reader is referred to the web version of this article.)

Fig. 3. Field views of coastal uplift during the 2010 Maule earthquake. Sites: a) ISYA; b) STN2; c) TUBU; d) LAVA.

of these estimates are based on a limited number of measurements, whose associated uncertainties were not systematically quantified.

3. Background and methods

3.1. Setting of P. purpuratus mussels

Perumytilus purpuratus (*Pp*) is one of the most common rocky mussels along the Pacific coast of South America from Ecuador to Cape Horn, extending over most of the Andean subduction margin (Osorio and Bahamonde, 1968; Alvarado and Castilla, 1996; Prado and Castilla, 2006; Carranza et al., 2009), as well as on the Atlantic coast of Patagonia (Bertness et al., 2006). *Pp* is the predominant competitor for primary substrate in the intertidal rocky coast of central Chile (Alvarado and Castilla, 1996), where it forms fringes or belts. At exposed coasts, *Pp* belts are distinctively centered in the middle intertidal zone (Fig. 4 and Fig. S1); belts are characterized by a high density of individuals covering up to 60% of the space with sharp limits and abrupt density gradients (e.g., Castilla and Duran, 1985; Ingólfsson, 2005). The habitat of *Pp*

resembles that of *Mytilus edulis*, a similar 'blue' mussel found in the North Pacific, European, and North Atlantic coasts (Bayne, 1976). Both species might extend over the entire intertidal zone, but the largest density of individuals is near mean sea level and sharp gradients in density occur at the upper and lower limits of the middle intertidal zone. Beyond these limits only scattered specimens are found in the lower and upper intertidal zones, usually along fractures (Haven, 1971; Ingólfsson, 2005).

The lower limit of *Pp* belts is controlled by predation, mostly by *Concholepas concholepas* (Castilla and Duran, 1985), an economically-important gastropod endemic to the coast of Chile and Perú harvested in the subtidal zone. Additionally, *Pp* is predated by *Heliaster* sp., a common starfish genus of the Pacific coast of South America (e.g., Paine et al., 1985). In wave-exposed coasts, the habitat of *Heliaster* is related to its size, with smaller specimens in high intertidal levels, and larger and older restricted to the lower intertidal zone (Manzur et al., 2010). Starfish control the lower intertidal distribution of mussels in temperate systems on both NE and SE Pacific coasts (Paine et al., 1985). In turn along the Atlantic coast of Patagonia, the *Pp* habitat might extend to the entire intertidal zone in wave-exposed sites due to inefficient predation, whereas in wave-protected settings it is restricted to the middle intertidal zone (Bertness et al., 2006). In the Pacific coast of South America and other temperate settings where predation efficiently limits *Pp* belts to the middle intertidal zone, land-level changes could be potentially estimated by leveling the post-earthquake elevation of *Pp* belts with respect to the new mean sea level.

3.2. *P. purpuratus* field survey

Robert FitzRoy, the captain of the Beagle, pioneered the use of intertidal organisms to estimate coseismic coastal uplift. He noticed that mussels at Santa María Island (location in Fig. 2, field view in Fig. 3b) had been uplifted during the great earthquake of February 20, 1835 (Fitzroy, 1839). This event also affected south-central Chile with an estimated magnitude of 8.5 (Lomnitz, 2004) and seems to have been similar to the 2010 event in terms of tsunami inundation, coastal uplift patterns, and distribution of intensities (Cisternas et al., 2010). FitzRoy visited Santa María twice, at the end of March and beginning of April, and although using rough survey methods reported "upheaval" of 2.4, 2.7, and 3 m, at the south, center, and north of the island, respectively. However, the type of mussel used by FitzRoy is not detailed in his notes as he speaks of "choros", the common name given in Chile for any kind of mussel. His tidal datum was also rather ambiguous as he referred to "recent high-water mark" and "spring-tide high-water mark" (Fitzroy, 1839). As a well-trained surveyor, FitzRoy extended his measurements to the uplifted coasts surrounding the Arauco Bay and Concepción areas (Fig. 2).

Eleven days after the 2010 Maule earthquake, we started a two-week survey to measure the elevation of *Pp* belts in the

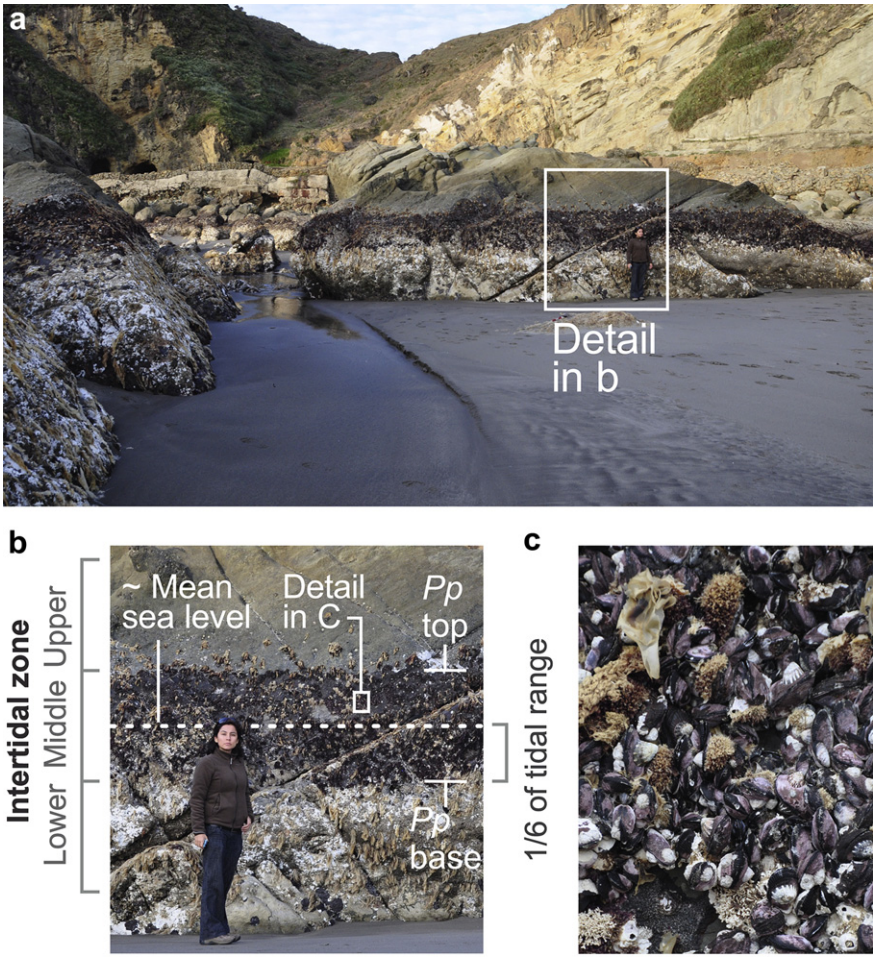

Fig. 4. Field views of the *Pp* belt. a) Overview of site LEB2. b) Detailed view of the belt indicating its limits. Note the sharp lower limit. The white coating that coves the exposed rocks below the belt is bleached coralline algae (*Lithothamnium*). c) Detail view of *Pp* mussels.

Arauco-Concepción region focusing on 33 sites along ~350 km of the coast (Fig. 2 and Fig. S2). At each site, we leveled the top and base of *Pp* belts in raised rocky outcrops exposed to waves (Figs. 3 and 4, Fig. S1) dispersed at an average of 50 m and maximum of 240 m (Fig. 5a). Measurements were restricted to exposed sites, avoiding sheltered locations such as tidal pools, channels, or estuaries. We used a GNSS (Global Navigation Satellite Systems) differential GPS system (Leica 1200) in rapid-static survey mode, and occasionally a conventional laser level mounted on a tripod. To minimize instrumental errors, we used a mobile GPS base station ensuring base-rover distances of less than 1 km, which allowed fixing all ambiguities and obtaining exclusively phase solutions. Base station coordinates were first calculated with respect to IGS (International GPS System) site CONZ at Concepción. Given the instrumental configuration, good weather conditions and satellite visibility, the elevation errors were found to be always below 1 cm.

To better assess the habitat of *Pp* with respect to our tidal model datum, we leveled *Pp* belts at two additional sites located beyond the earthquake rupture zone, and not affected by coastal land-level changes (CCTE and VALP). In order to minimize uncertainties in the tidal model datum at those sites, we deployed a portable ultrasonic tide gauge recording for ~10 h at 0.1 Hz sampling rate. A Gaussian filter was applied to remove noise associated with waves.

3.3. Tide levels and tidal model

In order to obtain the elevation of *Pp* belts with respect to post-earthquake mean sea level, at each site we surveyed tides as many times as possible over the longest achievable time interval obtaining a total of 212 tide levels. For those levels, absolute tide heights were computed using the TPXO 7.1 model (Egbert and Erofeeva, 2002), and all the *Pp* elevations were corrected to mean sea level. Where possible we selected sites sheltered from waves, usually at channels on broad emerged abrasion platforms (Fig. 3b and d). At those sites, tides were estimated with a reproducibility of less than 5 cm. On the contrary, in less sheltered sites exposed to strong southwesterly waves, tide levels reached differences of up to 1.1 m. Anyway, the difference between measured and modeled tide levels at all sites had a mean of 18 cm and standard deviation of 7 cm, suggesting a robust tidal correction to mean sea level. Tide levels and model fits for all sites can be found in the Supplementary materials (Fig. S5).

We compared tides predicted by two tidal models with real tide gauge measurements. Tides were calculated with the TPXO 7.1 (Egbert and Erofeeva, 2002) and XTide models (www.flaterco.com). TPXO is a predictive model, based on harmonic constituents extracted from 10 years of TOPEX/POSEIDON satellite altimetry data, whereas XTide estimates tides applying latitudinal offsets to harmonic constituents extracted from a nearby tide gauge base station. Though both models effectively predict ocean tides, nonharmonic influences on sea surface heights such as wind-related drag, the inverted barometer effect, or longer-term water temperature variations associated with El Niño-Southern Oscillation (ENSO) are not considered. These effects are well within the uncertainties of our model and thus have been discarded as done in similar studies (Meltzner et al., 2006).

Model tides were compared with data from a tide gauge station installed for engineering purposes at Santa María Island during June–July 2009 (Fig. S3). This station recorded tides using a digital pressure sensor recording at a 5-min interval, and was referred to the land benchmark SM1 installed by SHOA (the Oceanographic and Hydrographic Service of the Chilean Navy). The tide gauge data becomes noisy at high tides, most probably due to winter storm waves. In order to reduce this effect, we filtered the data using a running mean of 30 min. We found that residuals from the TPXO 7.1 model have a 10-cm lower standard deviation that those from the XTide model, suggesting the former reproduces tides better. TPXO has been successfully used in open ocean waters of the coast of northwestern Sumatra for similar purposes (Meltzner et al., 2006).

3.4. GPS estimates of coastal uplift

Coseismic displacements associated with the 2010 earthquake have been obtained from a few continuous and several campaign-type GPS stations distributed over the entire rupture zone (Vigny et al., 2011; Moreno et al., 2012). Campaign GPS monuments in south-central Chile started to be installed in the frame of the SAGA and CAP projects in 1994 (e.g., Klotz et al., 2001; Wang et al., 2007), LIA in 1996 (Ruegg et al., 2002, 2009), and SAGA-COGA in 2004 (Moreno et al., 2008, 2011, 2012). SAGA and COGA monuments were surveyed several times before the earthquake, last in December 2009, allowing for a good estimate of secular interseismic velocities used for linear extrapolation to the time of the earthquake (Moreno et al., 2012). The re-survey of GPS monuments started 6 days after the earthquake (Fig. S2b). In our study region, GPS measurements of coastal uplift range between 0.2 and 1.86 m,

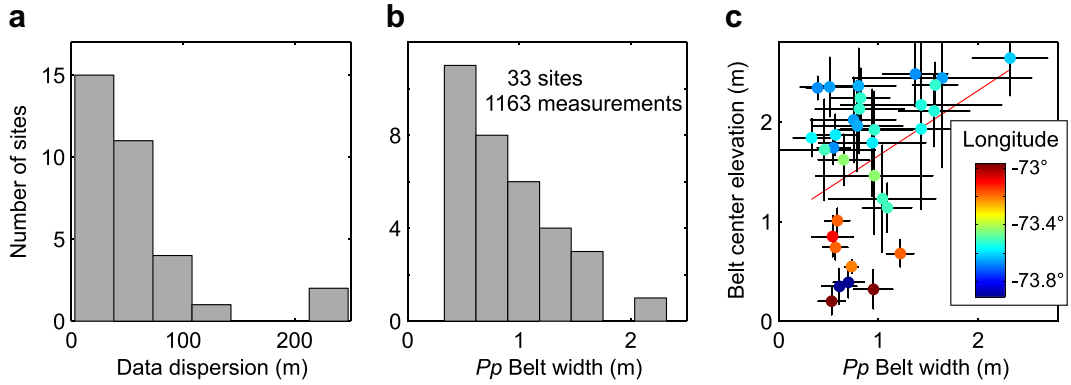

Fig. 5. Distribution of *Pp* belts. a) Dispersion of *Pp* measurements, the maximum distance between a single measurement and the center of all measurements at a particular site. b) Distribution of the *Pp* belt width. Theoretically, the belt occupies the middle intertidal zone and thus its width should equal 1/3 of the tidal range, 0.63 m in this region. The variability in belt width is associated with exposure to high waves (see Section 4.1). c) Relation between elevation of the *Pp* belt center and belt width. Both parameters tend to increase toward westernmost sites where coseismic uplift was largest and that are exposed to stronger waves at the open Pacific Ocean (Fig. 2).

with magnitudes decreasing away from the trench. Near the southern end of the rupture, the continuous GPS station at Mocha Island registered 0.2 m of uplift (Baez et al., 2010; Tong et al., 2010), while continuous stations on the northern rupture zone registered coastal subsidence (Vigny et al., 2011).

4. Results

4.1. Distribution of the P. purpuratus belt

Theoretically, along exposed coasts the *Pp* belt occupies the middle intertidal zone (e.g., Alvarado and Castilla, 1996). Thus, its vertical width should equal one third of the tidal range (Fig. 4b), and the belt center should be at mean sea level. The tidal range in the Arauco region is 1.9 m according to the 2009 tide gauge data (Fig. S3) and SHOA. If this relation stands, the elevation of the center of the *Pp* belt with respect to post-earthquake mean sea level would be a straightforward estimate of coseismic uplift. However, our data shows that belt width is about 1/3 of the tidal range (63 cm) at only 40% of the sites, and that belt width varies from 34 cm to 233 cm (Fig. 5b). Within error bounds belt width is below 1/3 of the tidal range only at two sites (LLIC and LEB1). Sites with higher belt width tend to correlate both with higher post-earthquake belt elevations and with their Longitude (Fig. 5c), which are representative of the distance to the trench and position with respect to the open Pacific coast, respectively (Fig. 2). Anyway, sites with reduced belt thickness also occur at lower Longitudes, and thus this variability renders the use of the belt center tenuous, as it is not uniformly distributed.

It has long been known that the vertical distribution of intertidal organisms can be affected by both climatic factors such as ENSO variations and global warming (e.g., Sagarin et al., 1999; Walther et al., 2002), site-specific issues such as the proximity to river mouths, coastal upwelling, and enhanced wave splash (e.g., Hobday, 1995; Ortlieb et al., 1996; Moreno et al., 1998), as well as oceanographic and anthropogenic factors controlling predation (e.g., Castilla and Duran, 1985; Paine et al., 1985; Castilla et al., 2004). Enhanced wave action results in a vertical expansion of the biozonation and thus the *Pp* belt could get wider upward, extending into the upper intertidal and even supratidal zones due to the continuous splash of seawater. Although we do not know of quantitative reports on this widening as a product of wave exposure, it is well known that wave exposure does control the recruitment and size of adult *Pp* (Alvarado and Castilla, 1996). Increased width due to wave exposure has been described for *Lithothamnium* and other intertidal species in northern Chile (Ortlieb et al., 1996) and the Pacific coast of North America (Hobday, 1995; Ramírez-Herrera and Orozco, 2002). Therefore uplift measured using the center of the *Pp* belt could be significantly overestimated in wave-exposed sites. This effect could explain the relation between belt width and belt center elevation with Longitude (Fig. 5c), as higher belts are located nearest to the trench at lower Longitudes along the western coast of the Arauco Peninsula (Fig. 2), which is exposed to the strongest waves in the region.

Understanding the variability of the *Pp* belt width is crucial to estimate coseismic uplift and to assess the uncertainties. A simple comparison of the belt top and base standard deviations at each site reveals clear differences: the mean standard deviations of the belt top is almost double that of the base, and this difference is also mimicked by the range of standard deviations (Fig. 6a). In order to visualize differences in the distribution of the belt for the entire data set, we subtracted the mean elevation of the belt top and base to every respective measurement at each site (Fig. 6b). This analysis further emphasizes the higher deviations from the mean of the belt top elevations. Nevertheless, both the entire data set of top and base deviations from mean elevations seem to be well described by

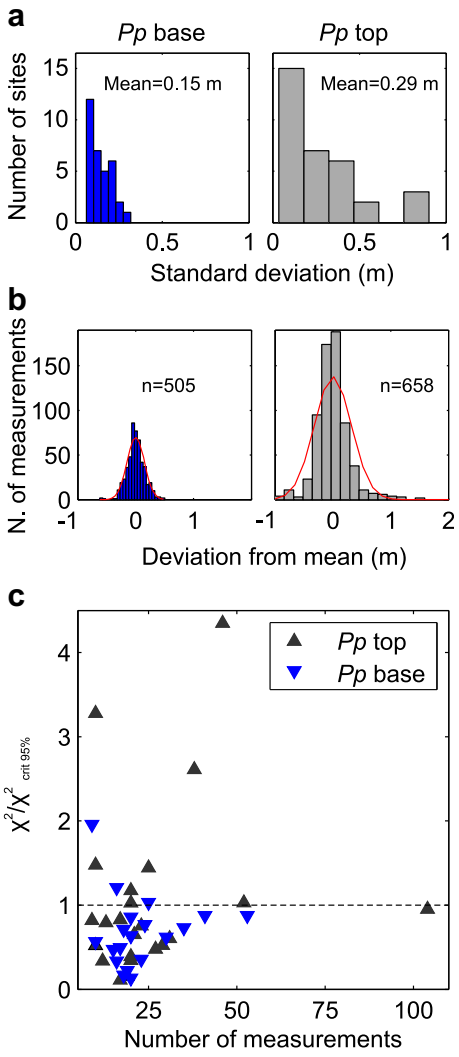

Fig. 6. Variability of *Pp* belts. a) Histograms of standard deviations at the 33 sites. Note higher and more disperse values for *Pp* tops. b) Histograms of deviation from the mean elevation of each site for the entire data set. Red curves show theoretical Gaussian distributions. Note higher deviations in *Pp* tops. c) Comparison of *Pp* belt base and top elevations with Gaussian distributions for each site with more than 8 measurements. Distributions are compared with the χ^2 parameter at 95% confidence. Sites with $\chi^2/\chi^2_{crit} < 1$ do not differ significantly from a Gaussian distribution. Comparatively, belt bases tend more toward Gaussian distributions than belt tops. Histograms showing *Pp* distributions at each site can be found in the Supplementary materials (Fig. S5). (For interpretation of the references to colour in this figure legend, the reader is referred to the web version of this article.)

Gaussian distributions (Fig. 6b), suggesting their mean represents a general tendency.

In an attempt to further quantify the variability of the *Pp* belt, we compared the distribution of belt top and base elevations with theoretical Gaussian distributions at each site. We used the χ^2 parameter at a critical confidence interval of 95%, and conducted this analysis for sites with at least 8 measurements of the *Pp* belt top or base following a standard methodology (Trauth, 2010). Distributions of the belt base are below the critical χ^2 for 84% of the analyzed sites but the belt top is below for only 65% of the sites (Fig. 6c). This suggests that more belt base distributions are not significantly different from Gaussian distributions, and thus that the mean and standard deviations are indicative of the tendency and dispersion of the population.

The higher variability in the distribution of the belt top with respect to its base is also suggested by higher maximum standard

deviations (Fig. 6a) and deviations from the mean (Fig. 6b). Our analysis corroborates previous inferences that wave action may control the upper range of intertidal organisms (e.g., Hobday, 1995; Ortlieb et al., 1996). Thus, the variability in *Pp* belt thickness observed in our entire data set (Fig. 5a) is mostly influenced by the unevenness of the belt top, an effect that can be also directly observed in the field (Fig. 4b and Fig. S1). Although sites with larger number of measurements tend to have lower $\chi^2/\chi^2_{critical}$ values (Fig. 6c), a particular correlation between these two parameters is not observed.

We calibrated the *Pp* belt base elevation with respect to our tidal model mean sea level at CCTE and VALP, located beyond the earthquake rupture (Fig. 7, Table 1). At both sites the continuous tide gauge records provide an excellent fit to the tidal model, with a standard deviation of 7 cm. The measurements have a $\chi^2/\chi^2_{critical}$ value <1 suggesting they follow Gaussian distributions. At both sites the mean elevation of the *Pp* base is coincident within uncertainties with the base of the middle intertidal zone. In addition, we back-corrected the position of the *Pp* base at TUBU by subtracting the amount of coseismic uplift determined independently from benchmark re-leveling (see Section 4.3 and Fig. 8). Although at this site the number of measurements is limited ($n = 8$), the mean elevation of the *Pp* base is also within the base of the middle intertidal zone.

4.2. Estimates of uplift with *P. purpuratus*

Because of the high variability in the *Pp* belt tops, using the elevation of the belt center with respect to post-earthquake mean sea level to estimate coastal uplift could result in significant bias. The variability in belt tops most likely result from local effects such as wave splash, which are difficult to quantify as they relate to bathymetry and topography as well as direction and intensity of ocean currents and winds. In an attempt to reduce this bias and based on the observation that *Pp* belt bases tend to follow a Gaussian distribution with a relatively narrow range of standard deviations and dispersion from the mean (Fig. 6a and b), we alternatively propose to use only the mean elevation of the belt base to estimate coseismic uplift. Because the *Pp* belt base mean elevation is located at the bottom of the middle intertidal zone (Figs. 7 and 8), the position of pre-earthquake mean sea level can be thus estimated by adding the mean post-earthquake belt base elevation and one sixth of the tidal range (32 cm in our study area). Uplift estimates using both approaches (belt center and belt base plus 1/6 tidal range) are shown in Fig. 9 and Table 1. We propagated the 2σ errors as:

$$2\sigma = \sqrt{(\text{ierr})^2+(\text{SD } Pp \text{ base})^2+(\text{SD } Pp \text{ top})^2+(\Delta\text{tide})^2}$$

where, ierr, the instrumental error is the uncertainty in dGPS processing results, SD *Pp* is the standard deviation of the belt base and top, and Δtide is the mean difference between measured and predicted tides (see Section 3.3). The third term has been omitted for estimates with only the belt base. A comparison of the belt center elevation and of the belt base plus 1/6 tidal range shows dissimilarities with a maximum difference of 84 cm (Fig. 9). The site with the largest discrepancy (RUME) is located at the western open coast of the Arauco Peninsula (Fig. 2) strongly impacted by waves.

4.3. Estimates of uplift with benchmarks re-leveling

The difference between the pre- and post-earthquake elevation of two benchmarks with respect to mean sea level was used to

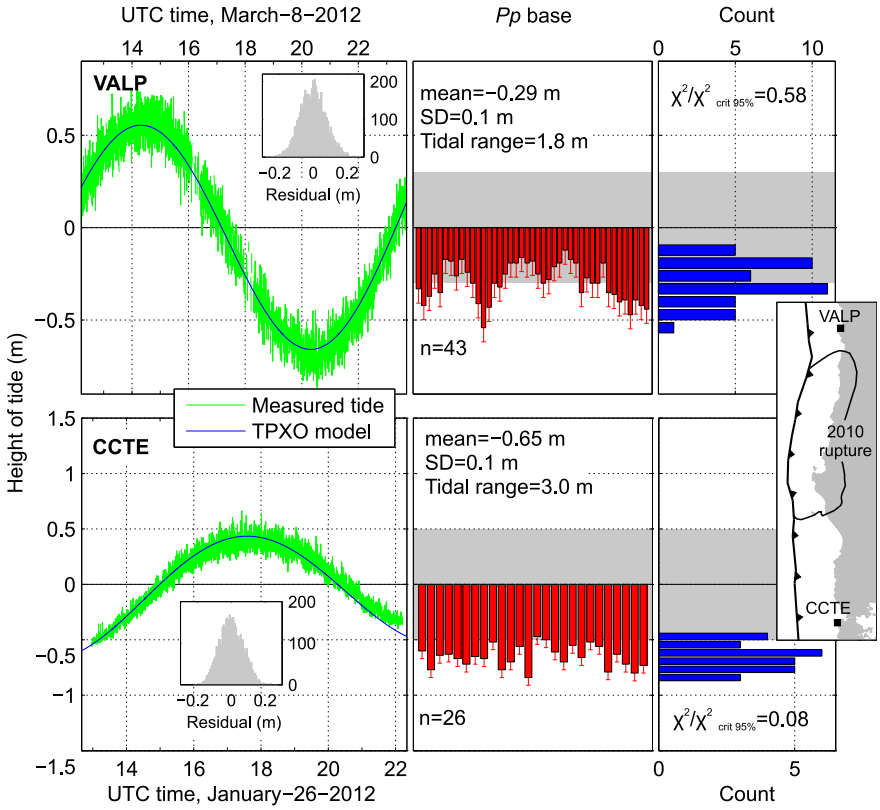

Fig. 7. Distribution of the *Pp* belt base at two calibration sites located beyond the earthquake rupture zone (Inset map shows location). The left panel shows tides surveyed with a portable tide gauge and modeled tides (Inset shows histogram of residuals). Center and right panels show *Pp* base elevations with respect to mean sea level, with 2σ error bars from tidal model fit. Gray rectangle denotes middle intertidal zone; at both sites the belt base is coincident with its base.

Table 1
Sites and *Pp* uplift results. Point dispersion is the maximum distance between a measurement and the center of all measurements at a given site. Errors are 2σ. Histograms and tide levels for each site can be found in the Supplementary materials (Fig. S5).

Site code	Reference locality	Longitude (°)	Latitude (°)	Elevation of *Pp* belt center (m)	Error (m)	*Pp* belt thickness (m)	Uplift (*Pp* base +1/6 TR) (m)	Error (m)	Number of *Pp* top	Number of *Pp* base	Number of tide levels	Day (March 2010)	*Pp* dispersion (m)
CORN	Coronel	−73.1762	−37.0282	0.69	0.13	1.22	0.40	0.10	19	20	12	21	43
ISYA	Islote Yani	−73.6667	−37.3577	1.75	0.16	0.55	1.79	0.12	27	30	9	26	106
LAVA	Lavapié	−73.5818	−37.1477	1.82	0.51	0.94	1.67	0.30	52	53	12	16	54
LEB2	Lebu	−73.6424	−37.5811	2.36	0.38	0.80	2.28	0.15	23	18	3	13	40
LIRQ	Lirquén	−72.9774	−36.7070	0.20	0.14	0.53	0.26	0.07	20	19	5	19	28
LLIC	Llico	−73.5643	−37.1914	1.84	0.19	0.33	1.99	0.10	31	17	7	16	64
MINA	Minca Costa	−73.6652	−37.6418	2.48	0.33	1.37	2.11	0.14	17	20	3	15	38
MOR1	Morguilla	−73.6623	−37.7228	2.35	0.30	0.51	2.41	0.23	20	24	9	15	43
MOR2	Morguilla	−73.6600	−37.7267	2.02	0.43	0.75	1.96	0.15	20	16	3	15	57
PENA	Las Peñas	−73.4294	−37.2393	1.46	0.59	0.96	1.30	0.09	10	10	5	17	14
PIUR	Piure	−73.6552	−37.2354	2.44	0.90	1.64	1.93	0.09	5	4	5	25	46
RUME	Rumena	−73.6154	−37.1750	2.64	0.38	2.32	1.80	0.20	29	41	4	25	248
SMD2	Las Dolores[a]	−73.5535	−37.0237	1.93	0.81	1.43	1.54	0.08	8	8	5	23	82
ST3C	Tres Cuevas[a]	−73.5222	−36.9997	2.37	0.23	1.57	1.90	0.11	10	5	6	11	34
STN1	Puerto Norte[a]	−73.5345	−36.9736	2.07	0.31	1.56	1.60	0.14	13	17	7	12	116
STN2	Puerto Norte[a]	−73.5431	−37.0065	2.17	0.81	1.43	1.77	0.07	8	8	8	23	82
STPS	Puerto Sur[a]	−73.5104	−37.0462	1.72	0.51	0.46	1.80	0.21	108	2	3	12	235
STS1	Punta Sur[a]	−73.5190	−37.0737	2.13	0.45	0.81	2.04	0.22	46	25	3	11	54
STS2	Punta Sur[a]	−73.5169	−37.0708	2.24	0.30	0.82	2.15	0.24	12	15	3	11	61
TIRU	Tirúa	−73.5053	−38.3410	1.14	0.25	1.09	0.91	0.17	17	23	8	14	95
TOME	Tomé	−72.9637	−36.6190	0.32	0.20	0.95	0.16	0.11	20	20	9	19	21
TROV	Trovolhue	−73.5074	−38.3633	1.23	0.54	1.04	1.03	0.17	8	7	8	14	23
TUBU	Tubul	−73.4366	−37.2264	1.63	0.25	0.65	1.62	0.22	5	8	11	16	7
YANS	Caleta Yani	−73.6383	−37.3731	1.96	0.46	0.79	1.88	0.18	38	35	13	25	65
MOC1	Isla Mocha	−73.9082	−38.4113	0.37	0.14	0.70	0.34	0.04	21	3	8	21	10
MOC2	Isla Mocha	−73.9170	−38.4102	0.33	0.16	0.61	0.34	0.04	25	3	8	21	14
CHIV	Chivilingo	−73.1839	−37.1530	0.74	0.13	0.57	0.78	0.08	7	7	3	17	25
CHOM	Chome	−73.2120	−36.7737	0.55	0.07	0.73	0.50	0.06	4	4	4	15	3
LAV2	Lavapié	−73.5823	−37.1479	1.87	0.21	0.57	1.91	0.16	9	9	4	16	33
LEB1	Lebu	−73.6648	−37.5965	2.34	0.12	0.39	2.46	0.10	3	3	3	13	40
LENG	Lenga	−73.1751	−36.7647	1.01	0.13	0.59	1.03	0.09	6	6	6	18	20
STLN	Puerto Norte[a]	−73.5250	−36.9714	1.92	0.39	0.96	1.76	0.25	18	10	4	12	35
TUMB	Tumbes	−73.0934	−36.6398	0.85	0.21	0.54	0.89	0.14	7	7	4	18	20
CCTE	Cocotué	−74.0009	−41.9267	–	–	–	–	–	–	26	4741	26[b]	45
VALP	Valparaíso	−71.6324	−33.0236	–	–	–	–	–	–	43	5041	8[b]	60

Pp — *Perumytilus purpuratus*. TR-Tidal range.
[a] Sites on Santa María Island.
[b] Surveyed in January and March 2012.

estimate uplift at Tubul (TUBU) and Santa María Island (STPS). The benchmark at Tubul was carved on a bedrock platform on January 17, 2010 (41 days before the earthquake) in the frame of a paleoseismological study and leveled against tides over a period of 9 h (field view in Fig. 3c). The position of the benchmark was not affected by the seismic shaking or the tsunami, and was re-leveled against the tide 16 days after the earthquake. The pre- and post-earthquake elevation with respect to mean sea level was obtained by fitting the respective tide level measurements to the TPXO model, resulting in an uplift of 1.49 ± 0.07 m. Tide levels and model fits are shown in Fig. 8.

The elevation of the benchmark SM1 installed by SHOA at Santa María Island above mean sea level was estimated in the 2009 tide gauge survey by leveling. This benchmark is located on a strong concrete wall of the peer in Puerto Sur, which was apparently undisturbed by seismic shaking or the tsunami judging from its horizontal position to within 10 cm. We surveyed the elevation of SM1 against the tide 12 days after the earthquake. Coseismic uplift of 1.8 ± 0.1 m was estimated by subtracting the elevation in the 2009 tide gauge survey from our estimate (post-earthquake tide levels in Fig. S5). The associated uncertainty includes the instrumental error and the mean difference in measured and predicted tides.

4.4. Estimates of uplift with high-resolution topography

At Punta Morguilla, on the southwestern tip of the Arauco Peninsula (Fig. 2), we compared a pre-earthquake Digital Terrain Model (DTM) at 1-m resolution obtained from airborne LiDAR (Light Detection And Ranging) data with post-earthquake dGPS tracks surveyed in kinematic and rapid-static modes (Fig. 11a). The histogram of the difference between the DTM and dGPS ($n = 1848$) dGPS points) shows a symmetric unimodal distribution with high kurtosis (Fig. 11b). The mean is 2.0 m, with 75% of the measurements below 2.1 m and 90% below 2.3 m. The pre-earthquake LiDAR data had been referred to mean sea level and we corrected the post-earthquake dGPS data to mean sea level using the tidal model and tide levels (Fig. S5). The tails of the uplift distribution (Fig. 11b) correspond to regions of high local relief at distances below the 1-m grid size of the DTM, mostly on the steep flanks of the bedrock platform where the *Pp* belt was measured.

5. Discussion

5.1. Uncertainties in the Pp method and site selection

Our analysis of the elevation of *Pp* belts revealed that local site effects may have a strong influence on belt thickness, especially on its top boundary; an influence difficult to constrain. Belt bases are controlled by predation and seem to occur at constant elevation with respect to mean sea level, as suggested primarily by results of our calibration sites (CCTE and VALP) located in areas not affected by the earthquake (Fig. 7), and also by back-correcting the coseismic uplift determined from independent data at TUBU (Fig. 8). Scattered *Pp* individuals might occur along cracks over the entire

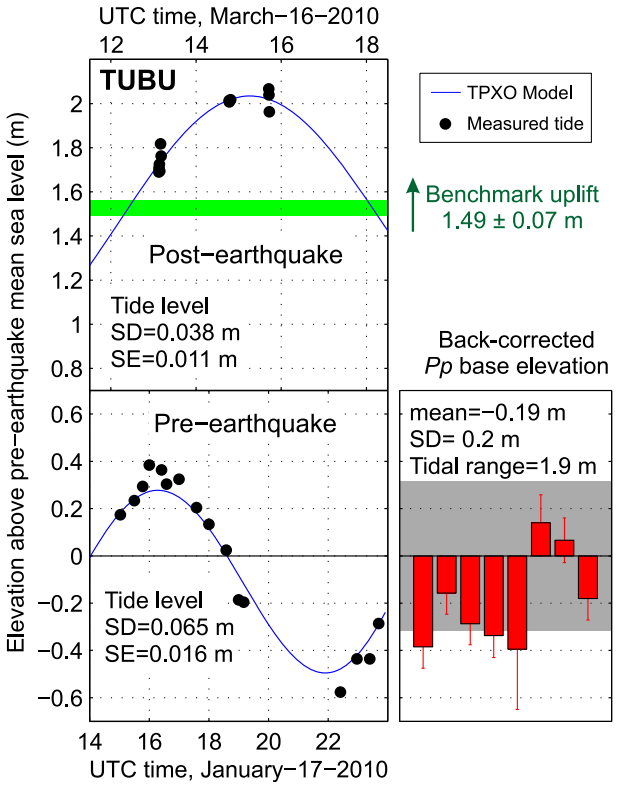

Fig. 8. Tide levels and modeled tides at site TUBU and post-earthquake measurements of the *Pp* base back-corrected to its pre-earthquake position using uplift determined from benchmark re-leveling. Error bars include 2σ uncertainties in dGPS measurements as well as pre- and post-earthquake tide leveling. Gray area denotes middle intertidal zone. SD-Standard deviation; SE-Standard error.

intertidal zone, but the highest densities occur within the middle intertidal zone. Measurements should be thus restricted to the sharp boundaries of the high-density zone, avoiding scattered individuals.

To overcome the bias introduced by unevenness in *Pp* belt tops and reduce the uncertainties, we propose to use only the *Pp* belt base to estimate coastal uplift. Thus, given that a considerable number of belt base measurements have been collected with

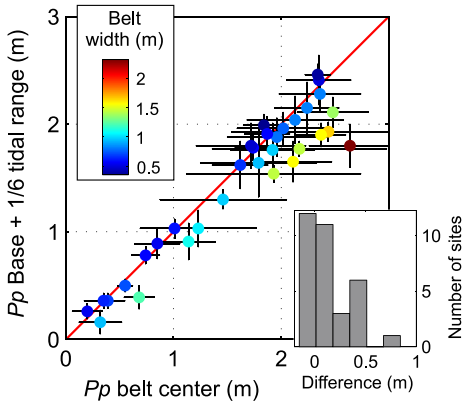

Fig. 9. Comparison of the post-earthquake elevation of the *Pp* belt center and belt base plus 1/6 of the tidal range. Theoretically, the *Pp* belt should be centered at mean sea level, but strong wave splash leads to a vertical expansion of the biozonation and thus higher belt tops. To overcome this bias, we propose to estimate coseismic uplift using the belt base elevation plus 1/6 of the tidal range. Inset shows histogram of difference between both estimates. Note that using the belt center may overestimate uplift by as much as 84 cm.

a homogeneous spatial distribution at a selected site, the main source of uncertainties will be the tide levels and tidal model. Assessing this uncertainty will depend on the number of tide levels and the time span between measurements. Tide leveling should be restricted to rocky platforms, preferably in tidal channels where wave-induced undulations of sea level are lowest; wave-breaking beaches should be omitted. The use of a portable tide gauge will significantly reduce the uncertainties in the tidal datum (Fig. 7). The comparison between modeled and surveyed tides during one month (Fig. S3) shows that phases are relatively well fitted, but that the model fails to reproduce the highest monthly amplitudes. Therefore, it is preferable to avoid measuring tide levels at those times. Leveling of *Pp* belts as well as of any other intertidal organism is clearly preferable during low tide, when accessibility to the bases will be easier, especially at sites that experienced low uplift.

The base of *Pp* belts is controlled by predation, thus, it is important to assess the impact that local processes such as overharvesting, pollution, and the oceanographic response to climate change might have on the habitat and diet of predatory species.

5.2. Comparison of different methodologies to estimate coastal uplift and assessment of their uncertainties

Coseismic coastal uplift associated with the 2010 earthquake has been estimated so far using: (1) a coralline crustose algae of the *Lithothamnium* group (Castilla et al., 2010; Farías et al., 2010; Vargas et al., 2011); (2) various intertidal organisms (Castilla et al., 2010); (3) a comparison of pre- and post-earthquake high-tide marks from interviews (Fritz et al., 2011); (4) campaign-type GPS measurements (Moreno et al., 2012; Vigny et al., 2011); (5) continuous GPS stations (Tong et al., 2010; Vigny et al., 2011); and (6) our estimates using *Pp*, benchmarks, and high-resolution topography.

All the above-mentioned data sets were obtained within the 55 days following the earthquake, a period during which post-seismic motions particularly rapid afterslip may occur after a great earthquake (e.g., Wang, 2007). Afterslip tends to surround the locus of maximum coseismic slip commonly resulting in vertical motions with a reverse polarity to coseismic displacements (e.g., Hsu et al., 2006). For example, our campaign GPS site STDO at Isla Santa María (location in Fig. 2) registered 1.8 m of coseismic uplift followed by about 0.15 m of post-seismic subsidence in the 50 days that followed the earthquake (Fig. S2a). We estimate that the maximum post-seismic subsidence in this time interval at sites of large coseismic uplift will not exceed ~10% of the coseismic uplift, although with strong spatial variations. Therefore the effect of afterslip will be well within the uncertainties of the methods using intertidal organisms and tide levels.

Lateral gradients in uplift are expected from the complex slip distribution of the 2010 earthquake (Tong et al., 2010; Pollitz et al., 2011; Vigny et al., 2011; Moreno et al., 2012). Thus, we compare uplift estimates from different methods only at collocated sites separated by a maximum distance of 4 km. Comparisons among the different methods and respective sources of error are discussed below and shown in Figs. 10 and 11.

5.2.1. Pp and GPS/leveling

For 13 sites this comparison has a relatively low standard error of 6.1 cm (Fig. 10a). The main uncertainties in campaign GPS displacements are: (1) the stability of the monuments. Seismically-induced ground shaking, soil compaction, liquefaction, landsliding, and other surface processes may alter the position of GPS monuments. Such effects might not be always easily recognized in the field, especially in densely vegetated regions such as the Maule rupture zone. (2) The linear

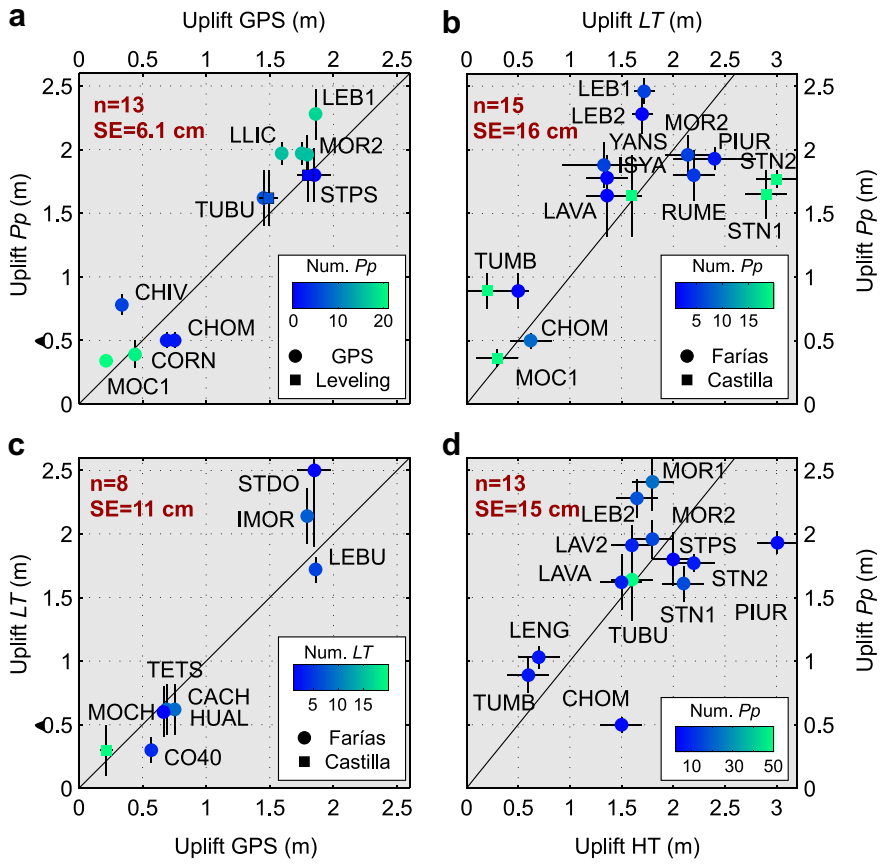

Fig. 10. Comparison of coseismic uplift estimated using different methods. Comparisons are made only for collocated sites separated by a maximum of 4 km. a) *Pp* with campaign GPS (Vigny et al., 2011; Moreno et al., 2012) and leveling (this study); b) *Pp* with *Lithothamnium* (*LT*) (Castilla et al., 2010; Farías et al., 2010; Vargas et al., 2011); c) *LT* with GPS (codes are of GPS sites); and d) *Pp* with high-tide marks (HT) (Fritz et al., 2011). The number of sites (*n*) and standard error (SE) for each compared data set is indicated in red. Color scales indicate number of measurements used to estimate uplift. (For interpretation of the references to colour in this figure legend, the reader is referred to the web version of this article.)

extrapolation of pre-earthquake measurements to the time of the earthquake. This might be a source of error in the data of Vigny et al. (2011), which was surveyed in 1996, 1999, and last before the earthquake in 2002 (Ruegg et al., 2009), providing only 3 measurements within 6 years for a 9 year-long extrapolation. Such an effect might explain the 15-cm difference in coseismic uplift estimated by different studies at Llico (Site LLI0 of Vigny et al. (2011) and LLIC of Moreno et al. (2012)). (3) Some continuous GPS stations record periodic seasonal variations in the vertical component, interpreted as a result of the water or snow loading cycle and the elastic response of the upper crust (e.g., Heki, 2001; Bevis et al., 2004). The amplitude of the seasonal signal is usually a few centimeters (up to 3 cm at site CONZ, Concepción), and removing it from campaign GPS results requires a dedicated modeling effort validated by a dense network of continuous stations. The same uncertainties apply for the leveling sites.

Our *Pp* estimates agree well with uplift recorded by the continuous GPS station at Mocha Island. However, this station is installed on a concrete pillar and not directly on bedrock. Because the pillar is embedded in a humid coastal wetland, soil compaction and liquefaction cannot be ruled out.

5.2.2. *Pp* and *Lithothamnium*

For 15 sites this comparison has a relatively high standard error of 16 cm (Fig. 10b). As a result of coastal uplift, *Lithothamnium* (*LT*) bleaches leaving a distinct white belt. Whereas the upper limit of this belt is usually sharp against bedrock (Fig. S1), its lower limit is transitional to the pinkish-colored living part of the crusty algae. The width of this transitional zone is controlled by tides and local wave splash, and is expected to decrease with time after the earthquake as the lowermost edge bleaches progressively.

The main source of error associated with *LT* measurements is thought to be enhanced wave splash, which extends its biozonation upwards (e.g., Ortlieb et al., 1996). At protected sites where the influence of wave splash is expected to be minimal (MOC1 and LAVA), the *LT* uplift estimates agree very well with *Pp* estimates. In turn, sites at the northern point of Santa María Island (STN1 and STN2), where the discrepancy between *Pp* and *LT* estimates is largest (up to 1.5 m) are most likely affected by wave splash. Local exposure to wave splash will not only influence the upper limit of the pre-earthquake *LT* belt, but also the width of the post-earthquake transitional zone between bleached and living *LT*. Thus, a large number of measurements per site may be needed to average these biases out, in different areas of the same site affected by different wave regimes. At each site, Castilla et al. (2010) made 25 measurements of the *LT* belt thickness that were averaged to estimate uplift. In turn, the estimates of uplift by Farías et al. (2010) are based on between 1 and 9 measurements per site, which might be a limiting factor in assessing the accuracy of their results. At some sites, the effect of wave splash can be observed in the field as a continuous oceanward increase in *LT* belt thickness along shore-normal outcrops (see Fig. 2 of Vargas et al., 2011). Sites where enhanced wave splash is suspected from such field observations should be discarded or sampled extensively.

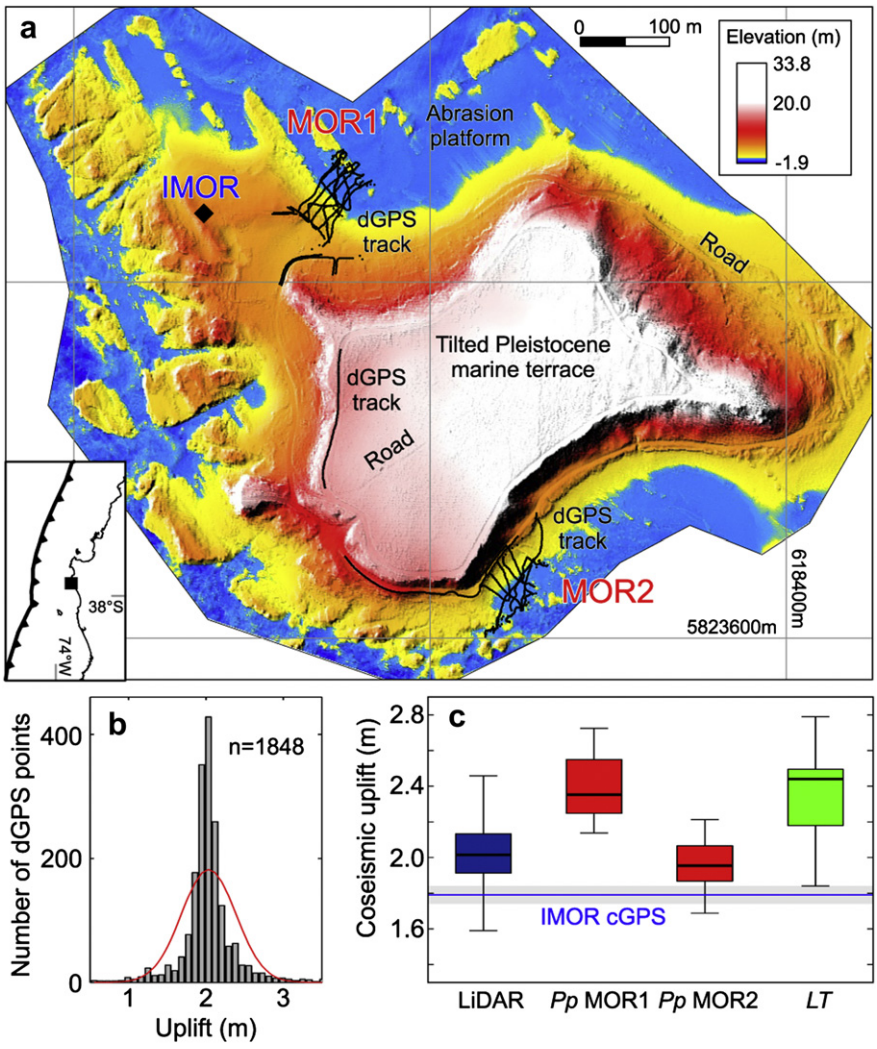

Fig. 11. Coseismic uplift at Morguilla. a) Pre-earthquake Digital Terrain Model (DTM) from airborne Light Detection And Ranging (LiDAR) at 1-m resolution. Black crosses show post-earthquake dGPS measurements. b) Histogram of uplift determined by subtracting dGPS from LiDAR elevations. Red line shows a theoretical Gaussian distribution. c) Box-and-whisker plots comparing coseismic uplift determined from: dGPS minus LiDAR; *Pp*; *LT* (Farías et al., 2010); and campaign GPS site IMOR (Moreno et al., 2012), location in a. (For interpretation of the references to colour in this figure legend, the reader is referred to the web version of this article.)

The main advantage of using *LT* with respect to *Pp* is the independence of the former from tidal models. In turn, the main disadvantage is the quantitative assessment of uncertainties associated with local site effects.

5.2.3. LT and GPS

For 8 sites this comparison has a standard error of 11 cm (Fig. 10c). This comparison includes site CO40 located north of our study region. The highest discrepancy is at site STDO, located at the western coast of the Santa Maria Island. This site is impacted by strong waves from the open Pacific Ocean, which most probably led to an overestimate of uplift with *LT*. In general, *LT* estimates at sites with lower magnitudes of uplift tend to agree better with GPS values. This is likely a result of enhanced wave splash occurring predominantly along the western coast of the Arauco Peninsula, where coseismic uplift was higher.

5.2.4. Pp and high-tide marks

For 13 sites this comparison has a relatively high standard error of 15 cm (Fig. 10d). Whereas pre-earthquake high-tide marks are usually well known by inhabitants, probably the most important source of error is the position of the post-earthquake counterparts. Although the earthquake occurred during full moon when tidal amplitudes are highest, the high-tide marks survey was conducted during the following half-moon period with reduced tidal amplitudes (Fig. S2b and S2c). Additionally, to recall the positions of precise high-tide marks, inhabitants likely need to observe at least several tidal cycles. Uncertainties associated with this method are difficult to quantify and the estimated error of 20 cm (H. Fritz, written communication, 2011) is probably a lower bound.

5.2.5. Pp, LT, GPS, and high-resolution topography at Morguilla

Morguilla offers the opportunity to compare various methodologies at the same site (Fig. 11c). The distribution of uplift determined by subtracting pre- from post-earthquake high-resolution topography is unimodal with a high kurtosis suggesting its mean is a significative estimate. The sources of uncertainty in this method are the absolute elevations with respect to mean sea level for both the pre- and post-earthquake data sets, which will only shift the distribution. The GPS site IMOR is installed in an uplifted abrasion platform of consolidated Eocene bedrock and no evident shaking-induced perturbation of the monument could be observed. IMOR

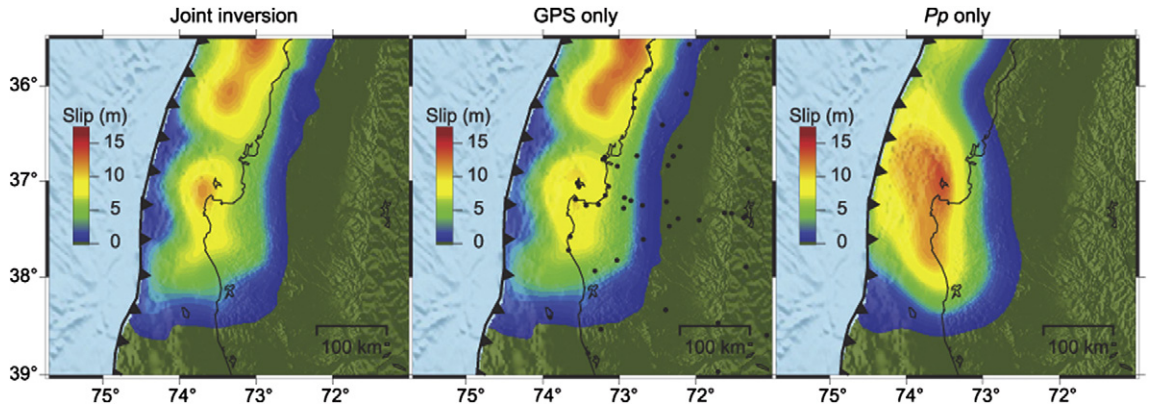

Fig. 12. Inversions for megathrust slip. The distribution of slip along the southern segment of the 2010 Chile earthquake estimated using the finite-element technique of Moreno et al. (2009). Black dots show location of GPS stations (Vigny et al., 2011; Moreno et al., 2012). Maps of uplift predicted by each method and residuals to each data set can be found in the Supplementary materials (Fig. S4).

was surveyed last in December 2009 and 6 days after the 2010 earthquake, thus limiting the uncertainty associated with extrapolation of the interseismic secular component.

The mean uplift estimated using *Pp*, *LT*, and LiDAR–dGPS exceeds the result from campaign GPS, and only the minimum range of values overlap (Fig. 11c). The large range in *LT* uplift results from including 8 measurements from different sites around the peninsula. Farías et al. (2010) discarded the higher values as the influence of enhanced wave splash was suspected. Uplift at MOR1 was constraint with 24 measurements of the *Pp* belt base and thus its mean should be representative. Higher uplift may result from inadequate tide levels, as the reproducibility of tide level at this site exposed to strong waves was low, with a range of 30 cm (Fig. S5). The dGPS data had been corrected to mean sea level using the same tide levels and thus it could also explain the slight difference with the GPS-determined uplift.

5.3. Contribution of *P. purpurata* uplift to distributions of megathrust slip and earthquake segmentation

The spatial distribution of megathrust slip may provide fundamental insight into the earthquake process. Most of the slip during megathrust earthquakes tends to occur offshore and thus its resolution and accuracy will rely on a high density of onshore data points. We have applied the 3D finite-element modeling inversion technique detailed in Moreno et al. (2009) using precise geometries of the megathrust, oceanic and continental Moho, as well as rheological parameters of each domain adapted from geophysical images and petrological studies (Tassara et al., 2006; Tassara and Echaurren, 2012). In order to gain insight into the contribution of intertidal organisms on estimates of megathrust slip, we made separate inversions using GPS and *Pp* data, and a joint inversion of both data sets (Fig. 12).

Because of the rather straight Chilean coastline, coastal uplift measurements are insufficient to perform a robust inversion for megathrust slip. Additionally, slip inversions along the low-dipping megathrust (10–20°) will be mostly sensitive to horizontal displacements provided by GPS vectors. For the southern segment of the 2010 rupture, the main difference between slip distributions derived only from GPS, and from GPS and *Pp* data is the shape of the southern slip maxima below the Arauco Peninsula (Fig. 12 and Fig. S4). Because this area was covered by only three GPS sites and outside the descending ALOS-Palsar swath used to obtain InSAR displacements (Tong et al., 2010; Vigny et al., 2011), slip distributions that exclude intertidal organisms provide minimum estimates for this region. Slip during the giant 1960 earthquake (M_w = 9.5), which mainly affected the segment of the megathrust to the south, extended across the Arauco Peninsula partly overlapping with the 2010 rupture (Moreno et al., 2009, 2011). Obtaining as much detail as possible in this region is important to gain insight into the segment boundaries of megathrust events (Fig. 12).

Our estimates of uplift reveal an interesting pattern along the southern edge of the 2010 rupture: uplift was higher at sites TIRU and TROV on the mainland with respect to Mocha Island (MOC1 and MOC2) located closer to the trench; and the highest uplift occurred between sites LEB2 and MOR2 along the southwestern sector of the Arauco Peninsula. Although these patterns can be explained by heterogeneously-distributed slip along the megathrust, they could be also associated with coseismic motion along the Morguilla fault system (Fig. 2). This structure consists of seismically-active reverse faults rooted in the plate interface, and extends along the southern edge of the Arauco Peninsula (Melnick et al., 2009). Sharp boundaries such as steep oblique crustal faults may act as geometrical barriers to propagation of seismic rupture along the megathrust, as has been proposed for a similar structure in southern Perú (Audin et al., 2008). Modeling studies combining geodetic and *Pp* data with complex fault geometries may provide further insight into the mechanisms associated with segmentation of megathrust earthquakes in this region.

6. Conclusions

This study analyzed the elevation of *Pp* mussels uplifted by the 2010 Maule earthquake (M_w = 8.8) that affected south-central Chile. In exposed rocky shores, *Pp* forms belts distinctively in the middle intertidal zone. We have shown that the base of *Pp* belts is at the bottom of the middle intertidal zone, and that it has a lower variability in elevation compared to belt tops. The high variability in belt tops is likely an effect of locally-enhanced wave splash. To overcome this bias, coastal uplift may be better estimated by using the mean base of the belts plus one sixth of the tidal range to reach mean sea level. This is supported by the fact that distributions of the belt base elevation are not significantly different from Gaussian distributions and thus its mean is representative of the general tendency. However, our approach relies on the use of a tidal model to refer the post-earthquake elevations to mean sea level, which is the main source of uncertainty. To minimize such errors, a large number of tide levels should be made over a long period of time in protected rocky platforms and away from wave-breaking beaches; preferably, a portable tide gauge device should be used.

Uplift estimates using *Pp* generally agree with GPS and benchmark re-leveling, but less well with estimates using *LT* and the

difference between pre- and post-earthquake high-tide marks from interviews. Discrepancies are likely associated with the lack of calibration studies, and in some cases a limited number of individual measurements averaged at each site. The main advantage of *Pp* is that local wave splash effects can be minimized.

For the 2010 earthquake, coastal uplift measurements using *Pp* increase the data density used to obtain a distribution of megathrust slip from joint inversions with geodetic data. The *Pp* data refines the slip distribution along the western coast of the Arauco Peninsula where the rupture zones of the 1960 ($M_w = 9.5$) and 2010 events overlap.

Because *Pp* is the predominant competitor for intertidal rocky coasts and has a wide latitudinal distribution, the methodology proposed here could have broad applications to survey land-level changes associated with earthquakes along the southeast Pacific as well as other temperate coasts.

Acknowledgments

This work was supported by grant ME 3157/2-1 of the German Science Foundation (DFG) to DM, Fondecyt N° 1110848 of the Chilean Science Foundation (Conicyt) to MC, and GFZ Potsdam. UNESCO rapidly financed post-earthquake fieldwork. A. Tassara provided the post-earthquake photo in Fig. 3d. The LiDAR data was provided by Digimapas Chile. We thank I. Urrutia and J. Jara for their help in the field, and R. Wesson for his portable tide gauge.

Appendix A. Supplementary material

Supplementary materials related to this article can be found online at doi:10.1016/j.quascirev.2012.03.012.

References

Alvarado, J., Castilla, J.C., 1996. Tridimensional matrices of mussels *Perumytilus purpuratus* on intertidal platforms with varying wave forces in central Chile. Marine Ecology Progress Series 133, 135–141.

Audin, L., Lacan, P., Tavera, H., Bondoux, F., 2008. Upper plate deformation and seismic barrier in front of Nazca subduction zone: the Chololo Fault System and active tectonics along the Coastal Cordillera, southern Peru. Tectonophysics 459, 174–185.

Awata, Y., Toda, S., Kaneda, H., Azuma, T., Horikawa, H., Shishikura, M., Echigo, T., 2008. Coastal deformation associated with the 2007 Noto Hanto earthquake, central Japan, estimated from uplifted and subsided intertidal organisms. Earth Planets and Space 60, 1059–1062.

Baez, J.C., Bataille, K., Tassara, A., Bevis, M., Kendrick, E., Vigny, C., Brooks, B., Smalley, R., Ryder, I., Parra, H., Moreno, M., Melnick, D., Barrientos, S., Blume, F., 2010. Co- and Post-seismic Surface Deformation Produced by the Maule Earthquake as Observed by a Dense Network of Continuous GPS Stations, AGU Fall Meeting, San Francisco, USA, pp. G33A-0840.

Bayne, B., 1976. Marine Mussels: Their Ecology and Physiology. Cambridge University Press.

Bertness, M.D., Crain, C.M., Silliman, B.R., Bazterrica, M.C., Reyna, M.V., Hildago, F., Farina, J.K., 2006. The community structure of ewstern Atlantic Patagonian rocky shores. Ecological Monographs 76, 439–460.

Bevis, M., Kendrick, E., Cser, A., Smalley, R., 2004. Geodetic measurement of the local elastic response to the changing mass of water in Lago Laja, Chile. Physics of the Earth and Planetary Interiors 141, 71–78.

Boding, P., Klinger, T., 1986. Coastal uplift and mortality of intertidal organisms caused by the September 1985 Mexico earthquakes. Science 233, 1071–1073.

Briggs, R.W., Sieh, K., Meltzner, A.J., Natawidjaja, D., Galetzka, J., Suwargadi, B., Hsu, Y.-J., Simons, M., Hananto, N., Suprihanto, I., Prayudi, D., Avouac, J.-P., Prawirodirdjo, L., Bock, Y., 2006. Deformation and slip along the Sunda megathrust in the great 2005 Nias-Simeulue earthquake. Science 311, 1897–1901.

Carranza, A., Defeo, O., Beck, M., Castilla, J.C., 2009. Linking fisheries management and conservation in bioengineering species: the case of South American mussels (Mytilidae). Reviews in Fish Biology and Fisheries 19, 349–366.

Carver, G.A., Jayko, A.S., Valentine, D.W., Li, W.H., 1994. Coastal uplift associated with the 1992 Cape Mendocino earthquake, Northern California. Geology 22, 195–198.

Castilla, J.C., Duran, L.R., 1985. Human exclusion from the rocky intertidal zone of central Chile: the effects on *Concholepas concholepas* (Gastropoda). Oikos 45, 391–399.

Castilla, J.C., Guiñez, R., Caro, A.U., Ortiz, V., 2004. Invasion of a rocky intertidal shore by the tunicate *Pyura praeputialis* in the Bay of Antofagasta, Chile. Proceedings of the National Academy of Sciences of the United States of America 101, 8517–8524.

Castilla, J.C., Manríquez, P.H., Camano, A., 2010. Effects of rocky shore coseismic uplift and the 2010 Chilean mega-earthquake on intertidal biomarker species. Marine Ecology – Progress Series 418, 17–23.

Castilla, J.C., 1988. Earthquake-caused Coastal Uplift and Its Effects on Rocky Intertidal kelp communities. Science 242, 440–443.

Cisternas, M., Melnick, D., Ely, L., Wesson, R., Norambuena, R., 2010. Similarities between the great Chilean earthquakes of 1835 and 2010. In: Atwater, B.F., Barrientos, S., Cisternas, M., Wang, K. (Eds.), AGU Chapman Conference on Giant Earthquakes and Their Tsunamis, Vina del Mar, Chile, p. 19.

Darwin, C., 1851. Geological Observations of South America. Smith, Elder, London.

Egbert, S.D., Erofeeva, S.Y., 2002. Efficient inverse modeling of barotropic ocean tides. Journal of Atmospheric and Oceanic Technology 19, 183–204.

Farías, M., Vargas, G., Tassara, A., Carretier, S., Baize, S., Melnick, D., Bataille, K., 2010. Land-level changes produced by the 2010 M_w 8.8 Chile earthquake. Science 329, 916.

Fitzroy, R., 1839. Proceedings of the second expedition, 1831–1836, under the command of Captain Robert FitzRoy. Volume II of Narrative of the Surveying Voyages of His Majesty's Ships Adventure and Beagle between the Years 1826 and 1836, Describing their Examination of the southern shores of South America, and the Beagle's circumnavigation of the globe, London, UK.

Fritz, H., Petroff, C., Catalán, P., Cienfuegos, R., Winckler, P., Kalligeris, N., Weiss, R., Barrientos, S., Meneses, G., Valderas-Bermejo, C., Ebeling, C., Papadopoulos, A., Contreras, M., Almar, R., Dominguez, J., Synolakis, C., 2011. Field survey of the 27 February 2010 Chile Tsunami. Pure and Applied Geophysics 168, 1989–2010.

Haven, S.B., 1971. Effects of Land-Level Changes on Intertidal Invertebrates, With Discussion of Postearthquake Ecological Succession, the Great Alaska Earthquake of 1964. National Academy of Sciences, Washington, pp. 82–126.

Hayes, G.P., Briggs, R.W., Sladen, A., Fielding, E.J., Prentice, C., Hudnut, K., Mann, P., Taylor, F.W., Crone, A.J., Gold, R., Ito, T., Simons, M., 2010. Complex rupture during the 12 January 2010 Haiti earthquake. Nature Geoscience 3, 800–805.

Heki, K., 2001. Seasonal modulation of interseismic strain buildup in northeastern Japan driven by snow loads. Science 293, 89–92.

Hobday, A., 1995. Body-size variation exhibited by an intertidal Limpet – influence of wave exposure, tidal height and migratory behavior. Journal of Experimental Marine Biology and Ecology 189, 29–45.

Hsu, Y.J., Simons, M., Avouac, J.P., Galeteka, J., Sieh, K., Chlieh, M., Natawidjaja, D., Prawirodirdjo, L., Bock, Y., 2006. Frictional afterslip following the 2005 Nias–Simeulue earthquake, Sumatra. Science 312, 1921–1926.

Ingólfsson, A., 2005. Community structure and zonation patterns of rocky shores at high latitudes: an interocean comparison. Journal of Biogeography 32, 169–182.

Klotz, J., Khazaradze, G., Angermann, D., Reigber, C., Perdomo, R., Cifuentes, O., 2001. Earthquake cycle dominates contemporary crustal deformation in central and southern Andes. Earth and Planetary Science Letters 193, 437–446.

Kölbl-Ebert, M., 1999. Observing orogeny – Maria Graham's account of the earthquake in Chile in 1822. Episodes 22, 36–40.

Konca, A.O., Hjorleifsdottir, V., Song, T.R.A., Avouac, J.P., Helmberger, D.V., Ji, C., Sieh, K., Briggs, R., Meltzner, A., 2007. Rupture kinematics of the 2005 M_w 8.6 m Nias–Simeulue earthquake from the joint inversion of seismic and geodetic data. Bulletin of the Seismological Society of America 97, S307–S322.

Lamarck, J.P.B.A., 1819. Histoire naturelle des animaux sans vertèbres. VI (1), 113. Verdière, Paris.

Lagabrielle, Y., Pelletier, B., Cabioch, G., RÈgnier, M., Calmant, S., 2003. Coseismic and long-term vertical displacement due to back arc shortening, central Vanuatu: offshore and onshore data following the M_w 7.5, 26 November 1999 Ambrym earthquake. Journal of Geophysical Research 108, 2519.

Lomnitz, C., 2004. Major earthquakes of Chile: a historical survey, 1535–1960. Seismological Research Letters 75, 368–378.

Manzur, T., Barahona, M., Navarrete, S.A., 2010. Ontogenetic changes in habitat use and diet of the sea-star *Heliaster helianthus* on the coast of central Chile. Journal of the Marine Biological Association of the United Kingdom 90, 537–546.

Meghraoui, M., Maouche, S., Chemaa, B., Cakir, Z., Aoudia, A., Harbi, A., Alasset, P.J., Ayadi, A., Bouhadad, Y., Benhamouda, F., 2004. Coastal uplift and thrust faulting associated with the M-w = 6.8 Zemmouri (Algeria) earthquake of 21 May, 2003. Geophysical Research Letters 31, L19605.

Melnick, D., Bookhagen, B., Strecker, M.S., Echtler, H.P., 2009. Segmentation of megathrust rupture zones from fore arc deformation patterns over hundreds to millions of years, Arauco peninsula, Chile. Journal of Geophysical Research 114, B01407.

Meltzner, A.J., Sieh, K., Abrams, M., Agnew, D.C., Hudnut, K.W., Avouac, J.-P., Natawidjaja, D.H., 2006. Uplift and subsidence associated with the great Aceh–Andaman earthquake of 2004. Journal of Geophysical Research 111, B10402.

Moreno, C.A., Asencio, G., Duarte, W.E., Marin, V., 1998. Settlement of the muricid *Concholepas concholepas* and its relationship with El Nino and coastal upwellings in southern Chile. Marine Ecology Progress Series 167, 171–175.

Moreno, M.S., Klotz, J., Melnick, D., Echtler, H., Bataille, K., 2008. Active faulting and heterogeneous deformation across a megathrust segment boundary from GPS data, south-central Chile (36–39°S). Geochemistry, Geophysics, Geosystems 9, Q12024.

Moreno, M.S., Bolte, J., Klotz, J., Melnick, D., 2009. Impact of megathrust geometry on inversion of coseismic slip from geodetic data: application to the 1960 Chile earthquake. Geophysical Research Letters 36, L16310.

Moreno, M.S., Rosenau, M., Oncken, O., 2010. 2010 Maule earthquake slip correlates with pre-seismic locking of Andean subduction megathrust. Nature 467, 198–202.

Moreno, M., Melnick, D., Rosenau, M., Bolte, J., Klotz, J., Echtler, H., Baez, J., Bataille, K., Chen, J., Bevis, M., Hase, H., Oncken, O., 2011. Heterogeneous plate locking in the South-Central Chile subduction zone: building up the next great earthquake. Earth and Planetary Science Letters 305, 413–424.

Moreno, M., Melnick, D., Rosenau, M., Baez, J.C., Klotz, J., Oncken, O., Tassara, A., Bataille, K., Chen, J., Socquet, A., Bevis, M., Bolte, J., Vigny, C., Brooks, B., Simons, M., Grund, V., Smalley, R., Carrizo, D., Bartsch, M., Hase, H., 2012. Toward understanding tectonic control on the M_w 8.8 2010 Maule Chile earthquake. Earth and Planetary Science Letters 321, 152–165.

Ortlieb, L., Barrientos, S., Guzman, N., 1996. Coseismic coastal uplift and coralline algae record in northern Chile: the 1995 Antofagasta earthquake case. Quaternary Science Reviews 15, 949–960.

Osorio, C., Bahamonde, N., 1968. Los moluscos bibalvos en las pesquerías Chilenas. Biología Pesquera 3, 69–128.

Paine, R.T., Castillo, J.C., Cancino, J., 1985. Perturbation and recovery patterns of starfish-dominated intertidal assemblages in Chile, New Zealand, and Washington State. The American Naturalist 125, 679–691.

Plafker, G., Savage, J.C., 1970. Mechanism of the Chilean earthquake of May 21 and 22, 1960. Geological Society of America Bulletin 81, 1001–1030.

Plafker, G., Ward, S.N., 1992. Backarc thrust faulting and tectonic uplift along the Caribbean Sea Coast during the April 22, 1991 Costa Rica earthquake. Tectonics 11, 709–718.

Plafker, G., 1965. Tectonic deformation associated with the 1964 Alaska earthquake. Science 148, 1675–1687.

Pollitz, F.F., Brooks, B., Tong, X., Bevis, M.G., Foster, J.H., Bŗgmann, R., Smalley Jr., R., Vigny, C., Socquet, A., Ruegg, J.-C., Campos, J., Barrientos, S., Parra, H., Soto, J.C.B., Cimbaro, S., Blanco, M., 2011. Coseismic slip distribution of the February 27, 2010 M_w 8.8 Maule, Chile earthquake. Geophysical Research Letters 38, L09309.

Prado, L., Castilla, J.C., 2006. The bioengineer *Perumytilus purpuratus* (Mollusca: Bivalvia) in central Chile: biodiversity, habitat structural complexity and environmental heterogeneity. Journal of the Marine Biological Association of the United Kingdom 86, 417–421.

Ramírez-Herrera, M.-T., Orozco, J.J.Z., 2002. Coastal uplift mortality of coralline algae caused by a 6.3 M_w earthquake, Oaxaca, Mexico. Journal of Coastal Research 18, 75–81.

Ruegg, J.C., Campos, J., Madariaga, R., Kausel, E., de Chabalier, J.B., Armijo, R., Dimitrov, D., Georgiev, I., Barrientos, S., 2002. Interseismic strain accumulation in south central Chile from GPS measurements, 1996–1999. Geophysical Research Letters 29, 1517.

Ruegg, J.C., Rudloff, A., Vigny, C., Madariaga, R., de Chabalier, J.B., Campos, J., Kausel, E., Barrientos, S., Dimitrov, D., 2009. Interseismic strain accumulation measured by GPS in the seismic gap between Constitucion and Concepcion in Chile. Physics of the Earth and Planetary Interiors 175, 78–85.

Sagarin, R.D., Barry, J.P., Gilman, S.E., Baxter, C.H., 1999. Climate-related change in an intertidal community over short and long time scales. Ecological Monographs 69, 465–490.

Subarya, C., Chlieh, M., Prawirodirdjo, L., Avouac, J.P., Bock, Y., Sieh, K., Meltzner, A.J., Natawidjaja, D.H., McCaffrey, R., 2006. Plate-boundary deformation associated with the great Sumatra–Andaman earthquake. Nature 440, 46–51.

Tassara, A., Echaurren, A., 2012. Anatomy of the Andean subduction zone: three-dimensional density model upgraded and compared against global-scale models. Geophysical Journal International. Online.

Tassara, A., Echaurren, A., 2012. Anatomy of the Andean subduction zone: three-dimensional density model upgraded and compared against global-scale models. Geophysical Journal International 189, 161–168.

Taylor, F.W., Briggs, R.W., Frohlich, C., Brown, A., Hornbach, M., Papabatu, A.K., Meltzner, A.J., Billy, D., 2008. Rupture across arc segment and plate boundaries in the 1 April 2007 Solomons earthquake. Nature Geoscience 1, 253–257.

Tong, X., Sandwell, D., Luttrell, K., Brooks, B., Bevis, M., Shimada, M., Foster, J., Smalley Jr., R., Parra, H., B·ez Soto, J.C., Blanco, M., Kendrick, E., Genrich, J., Caccamise II, D.J., 2010. The 2010 Maule, Chile earthquake: Downdip rupture limit revealed by space geodesy. Geophysical Research Letters 37, L24311.

Trauth, M., 2010. MATLAB Recipes for Earth Sciences, third ed. Springer.

Vargas, G., Farías, M., Carretier, S., Tassara, A., Baize, S., Melnick, D., 2011. Coastal uplift and tsunami effects associated to the 2010 M(w) 8.8 Maule earthquake in Central Chile. Andean Geology 38, 219–238.

Vigny, C., Socquet, A., Peyrat, S., Ruegg, J.-C., Metois, M., Madariaga, R., Morvan, S., Lancieri, M., Lacassin, R., Campos, J., Carrizo, D., Bejar-Pizarro, M., Barrientos, S., Armijo, R., Aranda, C., Valderas-Bermejo, M.-C., Ortega, I., Bondoux, F., Baize, S., Lyon-Caen, H., Pavez, A., Vilotte, J.P., Bevis, M., Brooks, B., Smalley, R., Parra, H., Baez, J.-C., Blanco, M., Cimbaro, S., Kendrick, E., 2011. The 2010 M_w 8.8 Maule mega-thrust earthquake of central Chile, monitored by GPS. Science 332, 1417.

Walther, G.-R., Post, E., Convey, P., Menzel, A., Parmesan, C., Beebee, T.J.C., Fromentin, J.-M., Hoegh-Guldberg, O., Bairlein, F., 2002. Ecological responses to recent climate change. Nature 416, 389–395.

Wang, K., Hu, Y., Bevis, M., Kendrick, E., Smalley Jr., R., Barriga-Vargas, R., Lauría, E., 2007. Crustal motion in the zone of the 1960 Chile earthquake: Detangling earthquake-cycle deformation and forearc-sliver translation. Geochemistry, Geophysics, Geosystems 8, Q10010.

Wang, K., 2007. Elastic and viscoelastic models of crustal deformation in subduction earthquake cycles. In: Dixon, T.H., Moore, J.C. (Eds.), The Seismogenic Zone of Subduction Thrust Faults. Columbia Press University, pp. 540–575.